



Contents lists available at ScienceDirect

# Construction and Building Materials

journal homepage: [www.elsevier.com/locate/conbuildmat](http://www.elsevier.com/locate/conbuildmat)

## Experimental study and numerical simulation of concrete pavement electrical heating for snow melting

Fang Wang<sup>a</sup>, Chaoliang Fu<sup>b,\*</sup>, Kai Liu<sup>c</sup>, Silu Huang<sup>d</sup>, Yangming Gao<sup>e</sup>, Hongzhou Xie<sup>f</sup><sup>a</sup> School of Civil Engineering, Anhui Jianzhu University, Hefei 230601, China<sup>b</sup> Institute of Highway Engineering, RWTH Aachen University, Aachen 52074, Germany<sup>c</sup> School of Automobile and Traffic Engineering, Hefei University of Technology, Hefei 230009, China<sup>d</sup> College of Civil Engineering, Nanjing Forestry University, Nanjing 210037, China<sup>e</sup> Built Environment and Sustainable Technologies (BEST) Research Institute, Liverpool John Moores University, Liverpool L3 3AF, United Kingdom<sup>f</sup> Chongqing Municipal Research Institute of Design, China

### ARTICLE INFO

#### Keywords:

Concrete pavement  
Snow-melting  
Snow-free ratio  
Electric heating pipe  
Finite element

### ABSTRACT

Road snow accumulation can lead to severe traffic delays, and commonly used deicing agents may pose potential environmental risks. Electrically heated concrete pavement systems utilizing heating pipe technology offer a safe and environmentally sustainable alternative. The snow-free ratio was frequently used as an evaluation index to evaluate the snow-melting performance in road infrastructure. However, the unique wavy temperature distribution during the snow-melting process of the heating system results in discontinuous melting, making the existing snow-free ratio inadequate for accurately assessing its performance and effectively guiding the operational strategy of the heating system. Therefore, this study analyzed the special temperature distribution and proposed a new calculation method for snow-free ratio based on the average temperature and the temperature non-uniformity coefficient of the pavement surface. First, the effects of factors such as heating pipe spacing, embedded depth, heating power, and wind velocity on average temperature and the temperature non-uniformity coefficient were analyzed using finite element simulation. Prediction models for average temperature and the temperature non-uniformity coefficient were then established and validated using the response surface method and experiments. Subsequently, using average temperature and the temperature non-uniformity coefficient as intermediate variables, a new functional relationship between the snow-free ratio and the four factors was established, allowing for satisfactory snow-melting performance to be achieved by adjusting the relevant factors of the heating system. The results show that the error rate between the proposed new calculation method and simulation results is only 4.44%. Moreover, it was concluded that adjusting spacing and heating power is the most effective strategy for heating systems to achieve optimal snow-melting performance.

### 1. Introduction

Concrete pavements play a pivotal role in transportation infrastructure by serving as key nodes in global connectivity. One of the main issues currently faced by concrete pavements is the high production costs and the significant environmental impact due to associated carbon emissions. To address these challenges, researchers are focusing on developing and using sustainable materials and enhancing recycling practices to reduce both the carbon footprint and production costs. For example, recycling materials such as rice straw ash [23,3], microsilica [14,35], and industrial waste [24,6] to partially replace cement concrete aggregates has yielded impressive results. Additionally, the safety of

driving on concrete pavements during nighttime and in snowy weather conditions is a significant challenge. Implementing Glow-in-the-dark [27,28] and plastic optical fibers markers [26] can enhance visibility, while developing effective snow and ice removal strategies can help maintain safer driving conditions on the concrete pavement during adverse weather [9,21,8]. This study primarily focuses on researching advanced snow-melting systems for concrete pavements to address the problem of road ice and snow accumulation. Global climate change is expected to cause more frequent extreme winter snowfall events, significantly impacting commuting by increasing delays and interruptions due to snow, ice, and slush on pavements ([22,25,2], Alsalou and Hotle. 2024). Traditional snow removal methods using chemicals and machinery are labor-intensive, time-consuming, and harmful to the

\* Corresponding author.

E-mail address: [fu@isac.rwth-aachen.de](mailto:fu@isac.rwth-aachen.de) (C. Fu).

<https://doi.org/10.1016/j.conbuildmat.2024.137611>

Received 7 June 2024; Received in revised form 9 July 2024; Accepted 24 July 2024

Available online 30 July 2024

0950-0618/© 2024 The Authors. Published by Elsevier Ltd. This is an open access article under the CC BY-NC-ND license (<http://creativecommons.org/licenses/by-nc-nd/4.0/>).

### Nomenclature

$A_r$	Ratio of the equivalent snow-free area to the equivalent snow-covered		
$\varphi$	Modified snow-free ratio		
$s$	Embedded spacing of the electric heating pipes (m)		
$d$	Embedded depth of the electric heating pipes (m)		
$L_1$	Length of the surface layer (m)		
$L_2$	Thickness of the surface layer (m)		
$n$	Number of the heating pipes		
$P_{1A}, P_{2A}, \dots, P_{(n-1)A}, P_n$	Points above the pipes		
$P_{1B}, P_{2B}, \dots, P_{(n-1)B}$	Points above the center line between two adjacent pipes		
$T_A$	Average temperature of the pavement surface ( $^{\circ}\text{C}$ )		
$C_n$	Standard deviation of the pavement temperature ( $^{\circ}\text{C}$ )		
$d_A$	Distance between $P_{iA}$ and the $i$ -th pipe ( $i=1, 2, \dots, n$ )	$\lambda_1, \lambda_2, \lambda_3$	Thermal conductivity of electric heating pipe, concrete and compacted snow ( $\text{W}/\text{m}\cdot\text{K}$ )
$d_B$	Distance between $P_{iB}$ and the $i$ -th pipe ( $i=1, 2, \dots, n$ )	$c_1, c_2, c_3$	Thermal capacity of the electric heating pipe, concrete and compacted snow ( $\text{J}/\text{kg}\cdot\text{K}$ )
$\Delta d$	Distance difference between $d_A$ and $d_B$	$\rho_1, \rho_2, \rho_3$	Density of the electric heating pipe, concrete and compacted snow ( $\text{kg}/\text{m}^3$ )
$D_s$	Thickness of the compacted snow (m)	$h$	Convective heat transfer coefficient ( $\text{W}/\text{m}^2\cdot\text{K}$ )
$P$	Heating power of the electric heating pipes ( $\text{W}/\text{m}$ )	$v$	Wind velocity (m/s)
$T_a$	Temperature of the environment (K)	$\alpha_1, \alpha_2, \alpha_3$	Coefficients for convective heat transfer coefficient calculation
$T_0$	Initial temperature of the model (K)	$\zeta$	Stefan–Boltzmann constant ( $\text{W}\cdot\text{m}^{-2}\cdot\text{K}^{-4}$ ), $\zeta = 5.669 \times 10^{-8} \text{ W}\cdot\text{m}^{-2}\cdot\text{K}^{-4}$
$q$	Rate of heat generation per unit area ( $\text{W}/\text{m}^2$ )	$\varepsilon$	Surface emissivity
$t$	Heating time (s)	$\varepsilon_{sky}$	Sky emissivity
$x, y$	Coordinate in the model.	$T_{sky}$	Effective sky temperature (K)
$T_1, T_2, T_3$	Temperature of the electric heating pipe, concrete and compacted snow (K)	$\Delta T_i$	Temperature difference between $T_i$ and $T_a$ (K)
		EHCPS-HPT	Electrically heated concrete pavement systems utilizing heating pipe technology
		EXP	Experimental results
		MCM	Monte Carlo Method
		PRE	Prediction results
		RSM-MCM	Response Surface Method-Monte Carlo Method
		SIM	Simulation results

environment and pavement structure, causing issues like concrete damage, drainage system corrosion, and soil ecological harm [11,7]. To address these problems, there is growing interest in replacing fossil fuel-powered operations and equipment with heating alternatives.

The heated concrete pavement systems (HCPS) primarily utilize heating wires, cables, and pipes as internal heat sources embedded near the pavement surface to transform electricity into radiant heat for snow melting. On the one hand, researchers have conducted extensive studies to investigate the effect of embedded spacing ( $s$ ), embedded depth ( $d$ ), heating power ( $P$ ) of heating sources, environmental factors, and power supply methods on the system's ice and snow melting efficiency and energy consumption. Zhao et al. [37] developed a concrete slab with carbon fiber heating wire for bridge deck deicing and concluded that at ambient temperatures ranging from  $-8^{\circ}\text{C}$  to  $-13^{\circ}\text{C}$ , the minimum input power required to completely melt ice layers of 2 mm, 5 mm, and 10 mm thickness within 3 h is 300  $\text{W}/\text{m}^2$ , 550  $\text{W}/\text{m}^2$ , and 800  $\text{W}/\text{m}^2$ , respectively. Lai et al. [16] investigated the snow-melting performance of airport pavement with carbon fiber grilles and found that an embedded depth of 5 cm and a spacing of 10 cm for the heat source are reasonable. They discovered that when the temperature ranges between  $-3^{\circ}\text{C}$  and  $-8^{\circ}\text{C}$  and the input power is 350  $\text{W}/\text{m}^2$ , the pavement temperature can increase by  $4.63^{\circ}\text{C}$  to melt a 2.7 cm thick layer of snow within 2 h. Liu et al. [20] investigated the operational efficiency of snow-melting concrete pavement by adjusting the  $s$ ,  $d$ ,  $P$  of heating pipes, and wind velocity ( $v$ ). They concluded that to decrease total heating time,  $s$ ,  $d$ , and  $v$  should all be decreased. To reduce the lost energy rate, both  $d$  and  $P$  should be increased, while  $s$  and  $v$  should be decreased. Daniels et al. [5] introduced an airport concrete pavement with embedded heating wires for anti-icing and compared two power supply methods. The alternating sequence energy supply method required longer heating times and did not save energy, while the automated thermostat sequence method achieved temperatures just above  $2^{\circ}\text{C}$  with lower power input. Jiao et al. [12] designed an electrical thermal pavement system embedded with heating wire and recommended the optimal  $s$  and  $d$  to be 10 cm and 4 cm, respectively. Meanwhile, as the heating power rose from 140  $\text{W}/\text{m}^2$  to 200  $\text{W}/\text{m}^2$  and

280  $\text{W}/\text{m}^2$ , the overall energy consumption increased by 22.39 % and 48.92 %, respectively. Conversely, the heating time required decreased by 21.80 % and 33.97 %, respectively.

On the other hand, to evaluate the snow and ice melting performance and energy consumption of heating systems, researchers often use the snow-free ratio ( $A_r$ ) as an evaluation index. Generally,  $A_r$  represents the percentage of days without snow cover over a specific period or the percentage of an area without snow cover over a specific area, with values ranging from 0 to 1. It is widely used in the monitoring and analysis of climate change, and the evaluation of snow-melting performance for building and transportation infrastructure. According to previous research [13,32], it is not necessary to design the heating system to achieve an  $A_r$  value of 1, as this would lead to energy waste. It is recommended that an  $A_r$  value of 0.5 be used for most heating system designs because this value provides adequate snow removal for normal conditions. Recently, Wang et al. [30] investigated the changes in  $A_r$  of concrete pavement with embedded heating pipes during the snow-melting process. They concluded that the melting process includes a starting period, a linear period, and an accelerated period, and found that an  $A_r$  value of 0.6 is reasonable for most traffic conditions. Similarly, Zhao et al. [39] introduced and discussed the impact of different pipe embedding depths (60, 80, and 100 mm) on the snow-free area ratio of a heating system with heat pipes at ambient temperatures ranging from  $-7.93$  to  $-9.36^{\circ}\text{C}$  and a snow thickness of 43 mm. They concluded that 80 mm is the optimal embedding depth, and the critical snow-free ratio designed for this condition should reach 0.7.

In summary, researchers have extensively studied the impact of layout parameters and operational parameters of heat source on the snow melting efficiency of HCPS, and the  $A_r$  was frequently used as an evaluation index to control these parameters. In general, the calculation of the  $A_r$  typically employs an image processing method to determine the  $A_r$  [10]. However, this approach is impractical for large-scale transportation infrastructure, and directly calculating the  $A_r$  to control heating system parameters requires significant time and effort. Moreover, even if a specific  $A_r$  value is determined, existing research has not quantified the relationship between  $A_r$  and EHCPS-HPT operational

parameters. As a result, it is challenging to directly adjust operational strategies to achieve the required  $A_r$ . More importantly, for the currently developed HCPS, the internal heat source arrangement in a wavy pattern can lead to faster snow melting in some local areas, resulting in discontinuous snow melting, as shown in Fig. 1 [38]. This makes accurately determining the snow-free ratio even more challenging. Therefore, it is essential to establish a method for calculating the snow-free ratio based on the unique temperature distribution characteristics and operational parameters of HCPS.

Given that, to bridge the knowledge gap and address technical bottlenecks, this study aims to develop a new method for calculating the  $A_r$  for application in practical engineering. As shown in Fig. 2, the first step is to build a simplified 2D snow-melting finite element model based on the EHCPS-HPT structure. For this simulation, the pipe's embedded spacing ( $s$ ), embedded depth ( $d$ ), heating power ( $P$ ), and wind velocity ( $v$ ) are selected as the parameters to investigate their impact on the average surface temperature  $T_A$  and temperature nonuniform coefficient  $C_n$  on the surface of EHCPS-HPT. The Monte Carlo Method (MCM) is used to analyze the sensitivity of these parameters. Based on the simulation results, prediction models for  $T_A$  and  $C_n$  are proposed using the response surface method, with the applicability of simulation and prediction models validated through experiments and variance analysis. Then, a new assessment metric  $\varphi$  is proposed, and its relationship with the  $A_r$  is established to derive a modified snow-free ratio function. The  $\varphi$  can be calculated from the simulation results. Finally, using  $T_A$  and  $C_n$  as intermediate variables, a new functional relationship between the  $\varphi$  and the four factors is established. This relationship is used to evaluate the snow-melting performance and predict the snow-free ratio of EHCPS-HPT, thereby guiding its operational strategies. If  $\varphi$  is 1, the operational parameters used in EHCPS-HPT are qualified. If  $\varphi$  is  $-1$ , it indicates that the above four parameters ( $s$ ,  $d$ ,  $P$ , and  $v$ ) need to be adjusted until they are qualified.

## 2. Establishment of finite element model and temperature field indicators of EHCPS-HPT

### 2.1. Structure of EHCPS-HPT

The schematic of the structure of EHCPS-HPT is shown in Fig. 3. The top layer is the cement concrete layer, and the electric heating pipes are evenly embedded in it. The insulating layer is between the cement concrete layer and the base course. This insulating layer serves to retard downward heat conduction, thereby minimizing energy loss.

### 2.2. Simplified model of EHCPS-HPT

To facilitate more efficient calculations, reasonable assumptions are made about the 3D structure to further simplify the model. Initially, due to the presence of the insulating layer, the heat transfer primarily occurs in the concrete layer. In this case, the analysis of the snow melting performance of EHCPS-HPT only considers the temperature distribution of the concrete layer. Furthermore, it is assumed that the heat generated

by the electric heating pipes is uniformly distributed along their length. Therefore, the 3D structure can be simplified to the 2D model shown in Fig. 4.

In addition, because the concrete layer is located above the insulation layer and the electric heating pipes are uniformly distributed, the bottom, left and right boundaries of the model are assumed to be adiabatic [17,31]. The upper boundary of the model considers thermal convection and thermal radiation. Meanwhile, the electric heating pipes, concrete, and snow in the model are assumed to be uniform, isotropic, and homogeneous. The heat transfer equation in the surface layer can be written as follows:

$$\frac{\partial^2 T_i}{\partial x^2} + \frac{\partial^2 T_i}{\partial y^2} - \frac{\rho_i c_i}{\lambda_i} \frac{\partial T_i}{\partial t} + \frac{q}{\rho_i c_i} = 0 \quad (1)$$

The initial condition is expressed as Eq. (2).

$$T_i(x, y, t)|_{t=0} = T_0, \quad i = 1, 2, 30 \leq x \leq L_1, \quad 0 \leq y \leq L_2 + D_s \quad (2)$$

The bottom, left and right conditions are expressed as Eq. (3).

$$\left. \frac{\partial T_1}{\partial x} \right|_{x=0} = \left. \frac{\partial T_1}{\partial x} \right|_{x=L_1} = \left. \frac{\partial T_1}{\partial y} \right|_{y=0} = 0 \quad (3)$$

The pavement surface conditions with or without a snow layer are expressed by Eqs. (4) and (5) [29].

$$\left. \frac{\partial T_2}{\partial y} \right|_{y=L_2} = h(T_2 - T_a) + \xi \varepsilon (T_{sky}^4 - T_2^4) = h \bullet \Delta T_2 + \xi \varepsilon (T_{sky}^4 - T_2^4) \quad (4)$$

$$\left. \frac{\partial T_2}{\partial y} \right|_{y=L_2+D_s} = h(T_3 - T_a) + \xi \varepsilon (T_{sky}^4 - T_3^4) = h \bullet \Delta T_3 + \xi \varepsilon (T_{sky}^4 - T_3^4) \quad (5)$$

$$T_{sky} = \varepsilon_{sky}^{0.25} \bullet T_a \quad (6)$$

where  $T_1$ ,  $T_2$  and  $T_3$  are the temperatures of electric heating pipe, concrete layer, and compacted snow, respectively (K);  $q$  is the rate of heat generation per unit area ( $\text{W}/\text{m}^2$ );  $\lambda_1$  ( $12.10 \text{ W}/\text{m}\cdot\text{K}$ ),  $\lambda_2$  ( $2.15 \text{ W}/\text{m}\cdot\text{K}$ ) and  $\lambda_3$  ( $1.03 \text{ W}/\text{m}\cdot\text{K}$ ) are the thermal conductivities of the electric heating pipe, concrete and snow ( $\text{W}/\text{m}\cdot\text{K}$ );  $\rho_1$  ( $7930 \text{ kg}/\text{m}^3$ ),  $\rho_2$  ( $2500 \text{ kg}/\text{m}^3$ ) and  $\rho_3$  ( $600 \text{ kg}/\text{m}^3$ ) are the densities of the electric heating pipe, concrete, and snow ( $\text{kg}/\text{m}^3$ ), and  $c_1$  ( $502 \text{ J}/\text{kg}\cdot\text{K}$ ),  $c_2$  ( $1004.8 \text{ J}/\text{kg}\cdot\text{K}$ ) and  $c_3$  ( $333697 \text{ J}/\text{kg}\cdot\text{K}$ ) are the thermal capacities of the electric heating pipe, concrete, and snow, ( $\text{J}/\text{kg}\cdot\text{K}$ ) [19].  $T_a$  is the ambient temperature (K);  $T_0$  is the initial temperature (K);  $D_s$  is the thickness of the compacted snow (m);  $\xi$  is the Stefan-Boltzmann constant ( $5.669 \times 10^{-8} \text{ W}\cdot\text{m}^{-2} \bullet \text{K}^{-4}$ );  $\varepsilon$  is the surface emissivity (0.90);  $T_{sky}$  is the effective sky temperature, and  $h$  is the heat transfer coefficient, which can be derived from Eq. (7).

$$h = 5.678 \times \left[ a_1 + a_2 \times \left( \frac{v}{0.304} \right)^{a_3} \right] \quad (7)$$

when  $0 \leq v \leq 4.88$ ,  $a_1 = 1.09$ ,  $a_2 = 0.23$ ,  $a_3 = 1$ ;

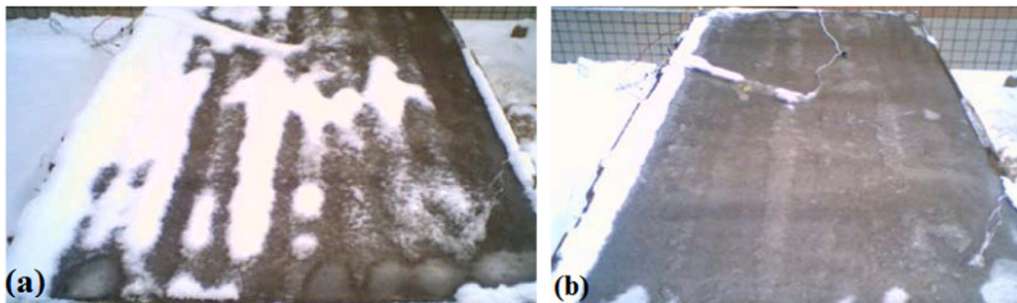


Fig. 1. The melting performance: (a) The discontinuous melting; (b) The melting is completed.

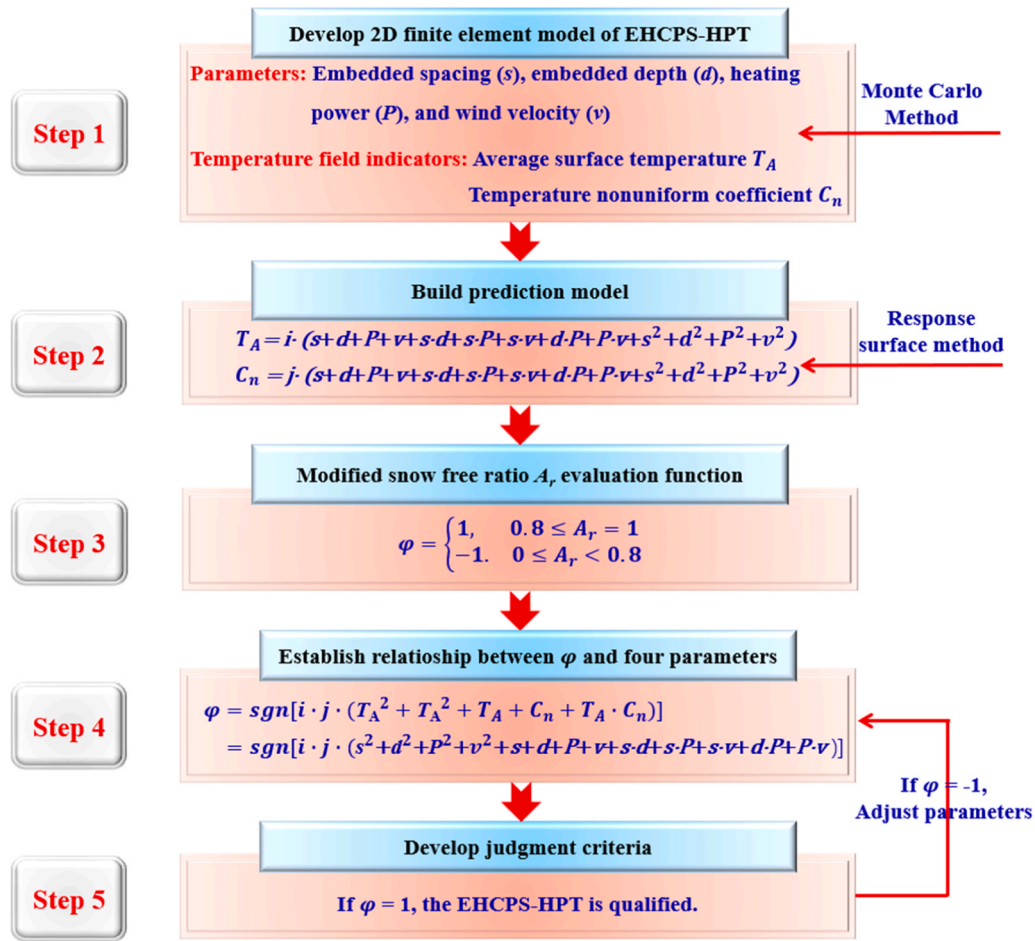


Fig. 2. The flow chart of new calculation method of snow-free ratio of this study.

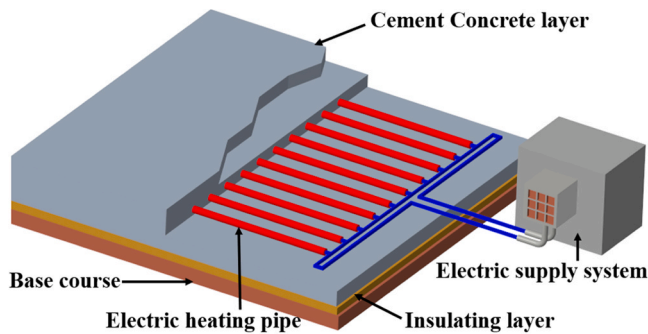


Fig. 3. The schematic of the structure of EHCPS-HPT.

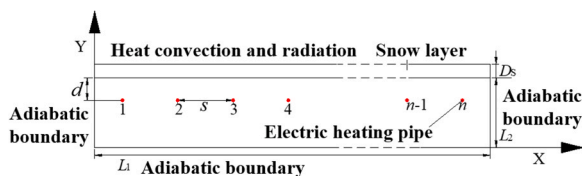


Fig. 4. Simplified model of EHCPS-HPT with the snow layer.

when  $4.88 \leq v \leq 30.48$ ,  $a_1 = 0$ ,  $a_2 = 0.53$ ,  $a_3 = 0.78$  [4].

### 2.3. Finite element model of EHCPS-HPT

The finite element simulations with different schemes are performed using ABAQUS, and a detailed FE meshing is constructed, as depicted in Fig. 5. The response surface method is applied in the scheme design for the simulation. According to the Specifications for Design of Highway Cement Concrete Pavement (JTG D40–2011), the  $s$  and  $d$  of the electric heating pipe should be 0.10 m–0.25 m and 0.06 m–0.12 m, respectively. The  $P$  was selected as the operational parameter, and  $v$  was considered an environmental factor. The detailed schemes are shown in Table 1. In addition, the simulations of EHCPS-HPT with different operational parameters were investigated within a heating time of 6 h and a snow layer thickness of 10 cm. This is because, if heavy snowfall continues for 6 h, the accumulated snow will hinder traffic and compromise safety [18]. Therefore, the EHCPS-HPT should start operating at the beginning of snowfall and should melt the snow to meet traffic requirements within 6 h. If the traffic requirements are not met, the EHCPS-HPT is considered

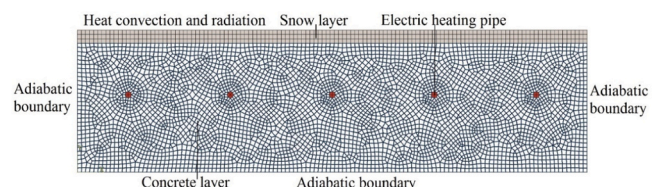


Fig. 5. Finite element meshing of EHCPS-HPT with the snow layer.

**Table 1**  
Simulation schemes based on response surface method.

Level	Influence factors			
	s (m)	d (m)	P (W/m)	v (m)
-2	0.10	0.06	20	0
-1	0.14	0.08	60	3.75
0	0.18	0.09	100	7.5
1	0.21	0.11	120	11.25
2	0.25	0.12	180	15
<b>Scheme</b>				
1	0.14	0.11	60	3.75
2	0.18	0.09	100	7.5
3	0.21	0.08	60	11.25
4	0.18	0.09	180	7.5
5	0.14	0.11	140	11.25
6	0.14	0.08	140	3.75
7	0.21	0.08	140	3.75
8	0.18	0.09	100	7.50
9	0.14	0.08	60	3.75
10	0.18	0.09	100	0.00
11	0.18	0.09	100	7.50
12	0.18	0.09	20	7.50
13	0.21	0.11	140	3.75
14	0.14	0.08	60	11.25
15	0.18	0.09	100	7.50
16	0.18	0.12	100	7.50
17	0.14	0.08	140	11.25
18	0.10	0.09	100	7.50
19	0.18	0.09	100	150
20	0.21	0.11	60	3.75
21	0.18	0.09	100	7.50
22	0.21	0.08	60	3.75
23	0.25	0.09	100	7.50
24	0.18	0.06	100	7.50
25	0.21	0.11	60	11.25
26	0.14	0.11	60	11.25
27	0.21	0.08	140	11.25
28	0.14	0.11	140	3.75
29	0.21	0.11	140	11.25
30	0.18	0.09	100	7.50

unqualified. Meanwhile, according to previous studies, the thickness of the accumulated snow is 10 cm after a heavy snowfall for 6 h [18]. In conclusion, the most unfavorable heavy snow conditions were chosen as the analysis conditions. The thickness of the accumulated snow (10 cm) and the heating time (6 h) are chosen for the melting analysis. Similarly, the conclusions obtained under these conditions can be used to evaluate and adjust the operational parameters of EHCPS-HPT for moderate and light snow conditions.

2.4. Development of temperature field indicators

In practical engineering, EHCPS-HPT is characterized by its considerable length and extensive coverage. Consequently, calculating the  $A_r$  demands significant time and effort. Moreover, even if a specific  $A_r$  value is determined, it is difficult to directly adjust the operation strategy to meet the qualification. Moreover, even if a specific  $A_r$  is determined, existing research has not quantified the relationship between  $A_r$  and EHCPS-HPT parameters. Therefore, it is difficult to directly adjust operational strategies to achieve the required  $A_r$ . More importantly, the pavement surface of EHCPS-HPT exhibits an uneven snow-melting

pattern, making it more challenging to accurately determine the snow-free ratio. This is due to the special layout method of heating pipes in EHCPS-HPT, as shown in Fig. 6.  $d_A$  is obviously less than  $d_B$ . Generally, the proximity to the heat source determines the amount of energy absorbed by a given point. Consequently, the temperature of  $P_{iA}$  is higher than that of  $P_{iB}$ , resulting in a wavy-like distribution of surface temperatures on the EHCPS-HPT. This wavy-like temperature distribution causes the accumulated snow on the low-temperature zones of the pavement surface to melt slowly or not at all, leading to a discontinuous snow-melting phenomenon.

In summary, the discontinuous snow-melting phenomenon arises from the amplitude and wavy-like distribution of temperatures across the pavement surface. Therefore, it is essential to identify temperature field indicators that are easy to monitor and can reflect the unique temperature distribution of EHCPS-HPT, thus indirectly and accurately calculating  $A_r$ . In this study, the average temperature  $T_A$  and the temperature nonuniform coefficient  $C_n$  were proposed as temperature field indicators to characterize temperature amplitude and distribution in finite element simulations. As shown in Fig. 6, points above the pipes ( $P_{1A}$ ,  $P_{2A}$ , ...,  $P_{(n-1)A}$ ,  $P_n$ ) and points above the centerline between two adjacent pipes ( $P_{1B}$ ,  $P_{2B}$ , ...,  $P_{(n-1)B}$ ) were selected. The temperatures of these points ( $T_{iA}$ ,  $T_{iB}$ , and  $T_n$ ) represent the pavement surface temperature. As shown in Eq. (8), the average value of these points' temperature is  $T_A$ , which reflects the predominant amplitude of the pavement surface thermal field.

$$T_A = \left[ T_n + \sum_{i=1}^{n-1} (T_{iA} + T_{iB}) \right] / (2n - 1) \tag{8}$$

The standard deviation is commonly employed to quantify the extent of data fluctuation. Consequently, in this study, the standard deviation of the selected points' temperature is defined as the temperature nonuniform coefficient  $C_n$ , calculated using Eq. (9).  $C_n$  serves to illustrate the temperature distribution across the thermal energy field on EHCPS-HPT.

$$C_n = \sqrt{\frac{(T_n - T_A)^2 + \sum_{i=1}^{n-1} [(T_{iA} - T_A)^2 + (T_{iB} - T_A)^2]}{2n - 1}} \tag{9}$$

3. Results and discussions

3.1. Effects of the single parameters on the temperature distribution

3.1.1. Embedded spacing

The effect of embedded spacing  $s$  on the average temperature  $T_A$  is illustrated in Fig. 7(a) and (b). It's evident that  $T_A$  decreases with increasing  $s$ , irrespective of other variables. This trend arises because, for a fixed pavement size, the number of heating pipes decreases as  $s$  increases. Fewer heating pipes mean less heating energy, leading to a decrease in  $T_A$ . However, the loss of energy due to convective heat transfer also decreases as  $T_A$  decreases. Consequently, the rate of decrease in  $T_A$  gradually diminishes as  $s$  increases.

The effect of  $s$  on the temperature nonuniform coefficient  $C_n$  is described in Fig. 7(c) and (d). It's observed that  $C_n$  initially decreases and then increases with increasing  $s$ , regardless of other variables. This phenomenon is attributed to the differing degrees of influence between the superposition of heat sources and the energy difference between  $P_{iA}$  and  $P_{iB}$ . When  $s$  is small, the central zone of the EHCPS-HPT surface experiences high temperatures due to the heat superposition of the heating pipes, resulting in a higher  $C_n$ . However, as  $s$  increases, the effect of heat superposition gradually weakens, leading to a decrease in  $C_n$ . Furthermore, as  $s$  continues to increase, the effect of the energy disparity between  $P_{iA}$  and  $P_{iB}$  becomes more pronounced. This energy difference is closely linked to the disparity in distance between  $P_{iA}$  and the heat source. As illustrated in Fig. 5, the distance difference between  $d_A$

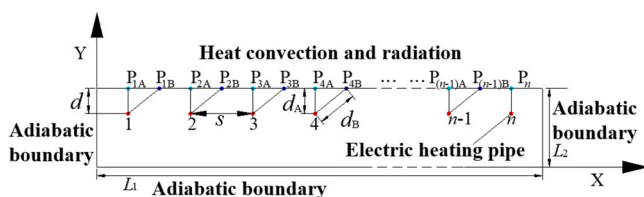


Fig. 6. Schematic of temperature distribution analysis.

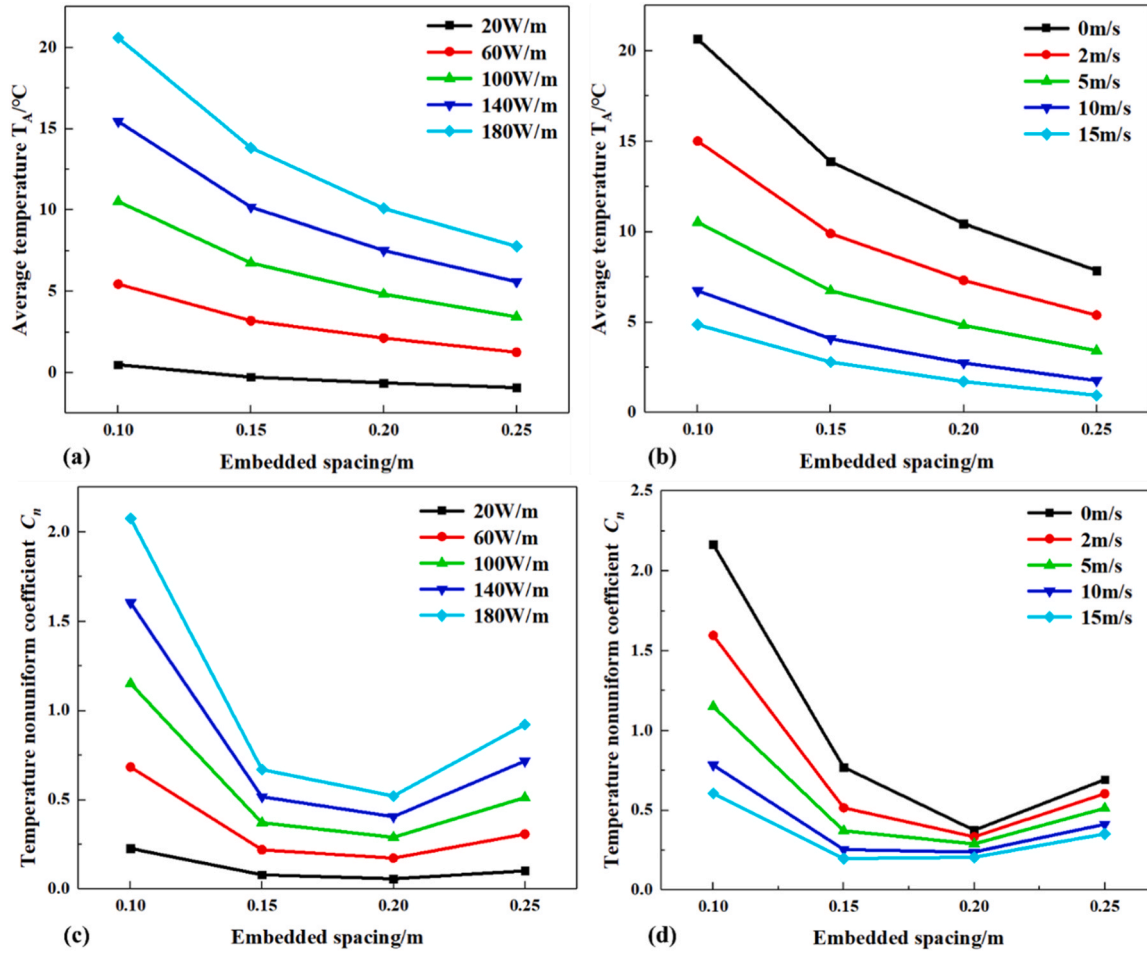


Fig. 7. The relationship between the characteristic variables and  $s$  with  $d=0.10$  m: (a)  $T_A$  variation with  $v=5$  m/s; (b)  $T_A$  variation with  $P=100$  W/m; (c)  $C_n$  variation with  $v=5$  m/s; (d)  $C_n$  variation with  $P=100$  W/m.

and  $d_B$  is denoted as  $\Delta d$ , as shown in Eq. (10). As  $\Delta d$  increases, so does the energy difference between  $P_{iA}$  and  $P_{iB}$ . From Eqs. (11)-(12),  $\Delta d'(s) > 0$  and  $\Delta d''(s) > 0$ , indicating that  $\Delta d$  increases with increasing  $s$ , and the rate of increase ( $\Delta d'$ ) also rises. Consequently,  $C_n$  initially decreases and then increases as  $s$  increases.

$$\Delta d = d_B - d_A = \sqrt{d^2 + \left(\frac{s}{2}\right)^2} - d \quad (10)$$

$$\Delta d'(s) = s/4 \sqrt{d^2 + \left(\frac{s}{2}\right)^2} \quad (11)$$

$$\Delta d''(s) = 4d^2 \sqrt{d^2 + \left(\frac{s}{2}\right)^2} / (d^2 + \left(\frac{s}{2}\right)^2)^2 \quad (12)$$

### 3.1.2. Embedded depth

The effect of embedded depth  $d$  on the average temperature  $T_A$  is illustrated in Fig. 8(a) and (b). It is evident that  $T_A$  diminishes as  $d$  increases due to reduced energy absorption by the pavement surface. With increasing  $d$ ,  $T_A$  experiences a gradual decline followed by a rapid decrease, irrespective of other variables. For example, under conditions where  $v = 0$  m/s, when  $d$  ranges from 0.06 m to 0.10 m,  $T_A$  decreases by 1.86°C with every 0.01 m increase in  $d$ . Similarly, within the range of 0.10 m to 0.12 m,  $T_A$  decreases by 4.39°C for every 0.01 m increase in  $d$ . This trend is attributed to the greater distance between the heat source and the point of measurement, leading to an accelerated rate of temperature decline [15].

In Fig. 8(c) and (d), temperature nonuniform coefficient  $C_n$  exhibits a similar trend to  $T_A$  but for different reasons. This phenomenon is attributed to the variation in  $\Delta d$ . As  $\Delta d$  decreases, the energy disparity between  $P_{iA}$  and  $P_{iB}$  decreases, consequently causing a decline in  $C_n$ . According to Eqs. (13)-(14),  $\Delta d'(d) < 0$  and  $\Delta d''(d) > 0$ . This implies that as  $d$  increases,  $\Delta d$  decreases, and the rate of decrease ( $\Delta d'$ ) amplifies. Consequently,  $C_n$  undergoes a gradual decline followed by a rapid descent.

$$\Delta d'(d) = \frac{d}{\sqrt{d^2 + \left(\frac{s}{2}\right)^2}} - 1 \quad (13)$$

$$\Delta d''(s) = s^2 \sqrt{d^2 + \left(\frac{s}{2}\right)^2} / 4(d^2 + s^2/4)^2 \quad (14)$$

### 3.1.3. Heating power

The effect of heating power  $P$  on the average temperature  $T_A$  and temperature nonuniform coefficient  $C_n$  is depicted in Fig. 9(a) and (b). It can be observed that both  $T_A$  and  $C_n$  exhibit a consistent upward trend with increasing  $P$ , regardless of other variables. As  $P$  increases, the energy absorbed by EHCPS-HPT intensifies, leading to a corresponding rise in  $T_A$ . This phenomenon stems from the linear relationship between temperature response and  $P$  in an infinite medium when other factors remain constant. Although the surface of EHCPS-HPT is subject to convective and radiative heat transfer, which can decrease  $T_A$ , the increase in  $P$  contributes more significantly to the rise in  $T_A$  than the

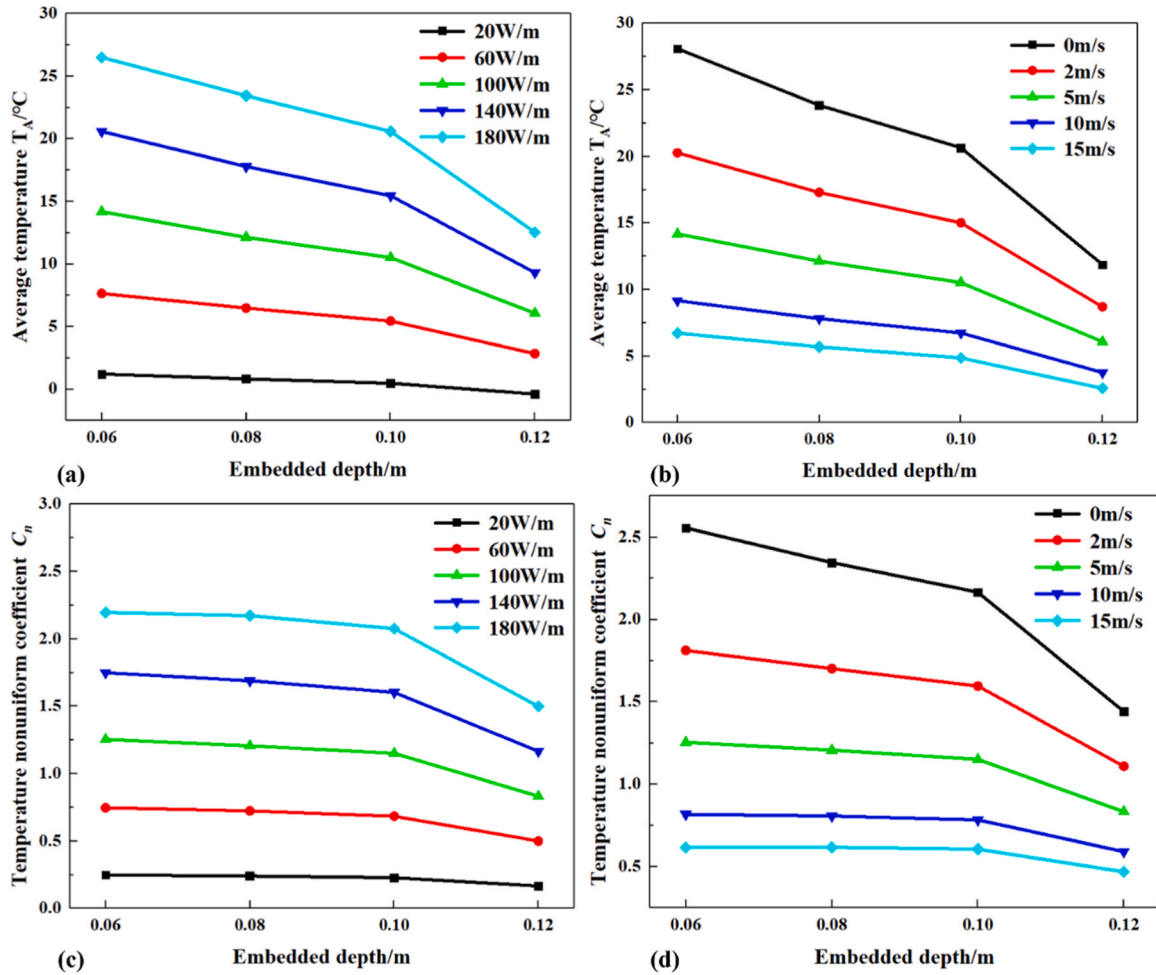


Fig. 8. The relationship between the characteristic variables and  $d$  with  $s=0.10$  m: (a)  $T_A$  variation with  $v=5$  m/s; (b)  $T_A$  variation with  $P=100$  W/m; (c)  $C_n$  variation with  $v=5$  m/s; (d)  $C_n$  variation with  $P=100$  W/m.

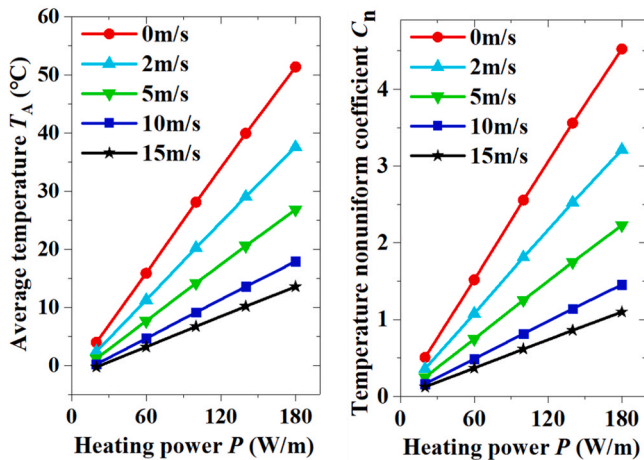


Fig. 9. The relationship between the characteristic variables and  $p$  with  $s=0.10$  m,  $d=0.06$  m: (a)  $T_A$  variation with  $t=6$  h; (b)  $C_n$  variation with  $t=6$  h.

convective and radiative heat transfer decreases it. As a result,  $T_A$  demonstrates nearly linear growth with increasing  $P$ . For the same reason,  $P_{iA}$  receives more energy than  $P_{iB}$ . Consequently,  $C_n$  also increases almost linearly.

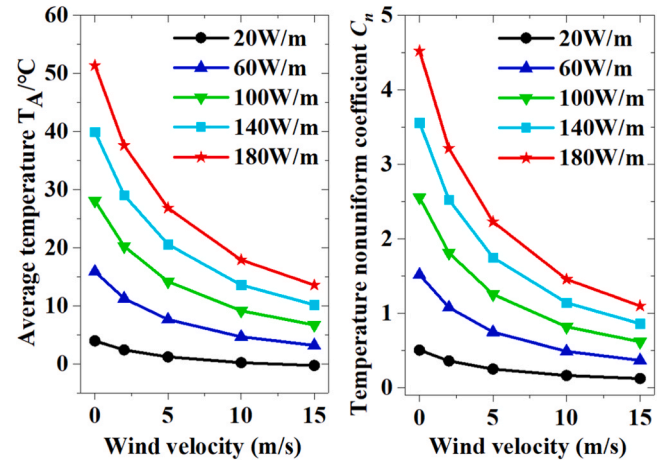


Fig. 10. The relationship between the characteristic variables and  $v$  with  $s=0.10$  m: (a)  $T_A$  variation with  $d=0.06$  m; (b)  $C_n$  variation with  $d=0.06$  m.

### 3.1.4. Wind velocity

The effect of wind velocity  $v$  on the average temperature  $T_A$  and  $C_n$  is described in Fig. 10 (a) and (b). It is evident that both  $T_A$  and  $C_n$  decrease, and this decline becomes less steep as  $v$  increases, regardless of other variables. As  $v$  increases, more energy dissipates into the environment, resulting in greater energy loss from the high-temperature

zone on the EHCPS-HPT surface. Consequently, the temperature difference between the high and low-temperature zones decreases, leading to a decrease in both  $T_A$  and  $C_n$  as  $v$  increases. Regarding the rate of decrease, the higher the  $v$ , the more active the heat transfer on the EHCPS-HPT surface, and the faster  $T_A$  and  $C_n$  tend to stabilize. In other words, when  $t$  is constant, the heat transfer at higher  $v$  is closer to a steady state, so the rate of decrease of  $T_A$  and  $C_n$  diminishes as  $v$  increases.

3.1.5. Sensitivity analysis of the parameters

The Response Surface Method-Monte Carlo Method (RSM-MCM) is utilized to explore the sensitivity of parameters, considering the influence of their range and randomness [1,36]. This method combines RSM to establish a prediction model and MCM to evaluate the simulation results of schemes listed in Table 1. According to Table 1, the parameters follow a normal distribution. The mean values of  $s$ ,  $d$ ,  $P$ , and  $v$  are 0.18 m, 0.09 m, 100 W/m, and 7.5 m/s respectively, with standard deviations of 0.03, 0.01, 36.39, and 3.41 respectively. For sensitivity analysis using RSM-MCM, partial correlation coefficients and contribution to variance are commonly employed to reflect parameter sensitivities.

The results of the sensitivity analysis are shown in Fig. 11. It can be observed that  $P$ ,  $v$ , and  $s$  are the primary parameters influencing  $T_A$ , with respective influence probabilities of 58.76 %, 23.92 % and 14.51 %. Additionally, from Fig. 11 (b), it is evident that  $v$  is the predominant parameter affecting  $C_n$ , with an influence probability of 96.6 %, significantly surpassing other parameters. In terms of the effects of parameters on  $T_A$  and  $C_n$ , a positive sensitivity value indicates a positive relationship, meaning  $T_A$  and  $C_n$  increase with the parameters' influence. Conversely, a negative sensitivity denotes a negative change in  $T_A$  and  $C_n$  with the parameter's influence.

In summary, the sensitivity analysis reveals that the behaviors of  $d$  and  $P$  align closely with those observed in the single-parameter analysis.  $T_A$  and  $C_n$  exhibit negative correlations with  $d$  and positive correlations with  $P$ . However, discrepancies emerge for  $s$  and  $v$  between sensitivity analysis and single-parameter analysis. In sensitivity analysis,  $C_n$  shows a negative correlation with  $s$ , whereas in single-parameter analysis,  $C_n$  initially decreases and then increases with  $s$ . Conversely,  $C_n$  exhibits a positive correlation with  $v$  in sensitivity analysis, contrasting with its decrease observed in the single-parameter analysis as  $v$  increases. This disparity may stem from the reliance on single-parameter analysis on fixed parameters, while sensitivity analysis assesses the collective influence of all parameters on the output simultaneously [34, 33]. In engineering applications, parameter adjustments often involve fixing other parameters. Therefore, the measures for parameter adjustment can follow the findings of single parameter analysis, while the priorities for adjusting the parameters should follow the results of sensitivity analysis.

3.2. Establishment and validation of prediction models of temperature distribution

3.2.1. Establishment of prediction models

In this section, a quadratic response surface method is used to analyze the relationship between  $T_A$ ,  $C_n$  and four influencing parameters ( $s$ ,  $d$ ,  $P$ ,  $v$ ). Based on the outcomes of thermal simulations conducted with the schemes listed in Table 1, the prediction models for  $T_A$  and  $C_n$  are obtained using RSM and are shown as follows:

$$T_A = 17.357 - 114.192s - 79.876d + 0.241P - 1.72v + 313.481s$$

$$\bullet d - 0.468s \bullet P + 3.214s \bullet v - 0.501d \bullet P + 3.939d \bullet v - 0.005P$$

$$\bullet v + 179.016s^2 - 14.405d^2 - 0.000013P^2 + 0.05v^2$$

$$C_n = 86.751 - 468.936s - 1984.346d + 0.041P - 0.27v + 11055.028s$$

$$\bullet d - 0.1s \bullet P + 0.699s \bullet v - 0.117d \bullet P + 0.585d \bullet v - 0.001P$$

$$\bullet v - 63.633s^2 + 10950.11d^2 + 0.06v^2 - 61139.383s \bullet d^2$$

Fig. 12 shows the comparison between the simulation results and prediction results. From Fig. 10 (a) and (b), it can be seen that the points align closely along a straight line, and the R-squared and Adjusted R-squared values are close to 1.

The analysis of variance (ANOVA) results for  $T_A$  and  $C_n$  are presented in Table 2. In ANOVA, the F-value and p-value serve as the primary assessment criteria, with a higher F-value and a lower p-value indicating greater significance of the corresponding parameter. A p-value less than 0.05 signifies significance, while values below 0.01 and 0.001 indicate high and extremely high significance, respectively. As shown in Table 2, the prediction models for  $T_A$  and  $C_n$  exhibit extremely high significance, with p-values less than 0.0001. In summary, the statistical analysis outcomes affirm the accuracy and reliability of the prediction models.

3.2.2. Validation of prediction models

To validate both the numerical model and the prediction models, experiments were conducted using cement concrete slabs to represent EHCPS-HPT, following the guidelines outlined in JTG D40-2011. The mix proportions for 1 m<sup>3</sup> of cement concrete were as follows: Portland cement (373 kg), limestone coarse aggregates (5-20 mm: 663 kg, 20-30 mm: 588 kg), tap water (153 kg) and quartz sands (373 kg). Electric heating pipes were embedded in the mold, and the cement concrete was then cast into the mold. Each slab measured 1 m×1 m×0.25 m. The different embedded schemes of electric heating pipes are presented in Table 3. Except for the top surface, all sides and the bottom of the slabs were wrapped with a 50 mm thick heat-insulating foam layer. Temperature measurement points were marked with 'X' as indicated in Fig. 13(a). The spacing between adjacent measuring points was  $s/2$ . In Fig. 13(a), for identical X coordinates, the average temperature of the measuring points was considered as the

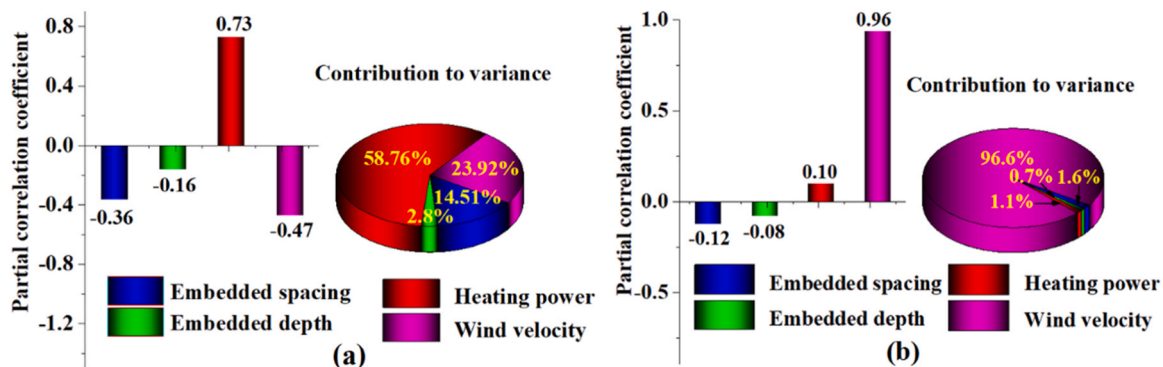


Fig. 11. The sensitivity analysis results based MCM: (a) The sensitivity analysis results for  $T_A$ ; (b) sensitivity analysis results for  $C_n$ .

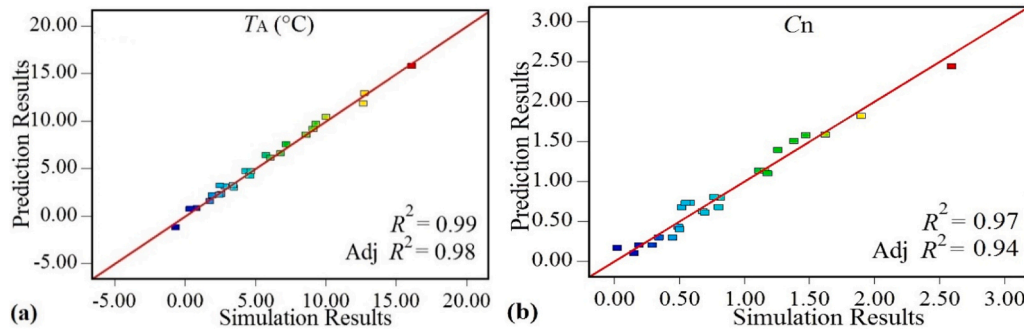


Fig. 12. The statistical analysis results of the prediction models: (a) The plot of the prediction results versus simulation results for  $T_A$ ; (b) The plot of the prediction results versus simulation results  $C_n$ .

Table 2  
Analysis of variance (ANOVA) for  $T_A$  and  $C_n$ .

Type	$T_A$		Type	$C_n$	
	F-value	p-value		F-value	p-value
$s$	308.0225	< 0.0001	$s$	8.8873	0.0093
$d$	53.9657	< 0.0001	$d$	43.3817	< 0.0001
$P$	875.8644	< 0.0001	$P$	166.1503	< 0.0001
$v$	478.6450	< 0.0001	$v$	61.233	< 0.0001
$s-d$	2.1420	0.1640	$s-d$	0.7136	0.4115
$s-P$	33.9838	< 0.0001	$s-P$	20.4207	0.0004
$s-v$	14.0746	0.0019	$s-v$	8.7307	0.0098
$d-P$	6.2266	0.0247	$d-P$	4.4733	0.0516
$d-v$	3.3813	0.0858	$d-v$	0.979	0.3381
$P-v$	42.1251	< 0.0001	$P-v$	5.9724	0.0274
$s^2$	7.4843	0.0153	$s^2$	12.6724	0.0029
$d^2$	0.0012	0.9724	$d^2$	5.0362	0.0403
$P^2$	0.0485	0.8286	$v^2$	11.9445	0.0035
$v^2$	58.4504	< 0.0001	$s-d^2$	80.2191	< 0.0001
Model	134.5322	< 0.0001	Model	34.4238	< 0.0001

Table 3  
Embedded schemes of electric heating pipes.

Slab	Embedded spacing $s$ (m)	Embedded depth $d$ (m)	Number of pipes
No.1	0.16	0.08	7
No.2	0.20	0.08	5
No.3	0.16	0.10	7
No.4	0.20	0.10	5

surface temperature of the corresponding position in the 2D model depicted in Fig. 5. The surface temperature was measured every hour during heating as shown in Fig. 13(b). Snow-melting experiments were conducted as illustrated in Fig. 13(c). The mass of melted snow was determined by weighing the water collected in the container.

Fig. 14(a) illustrates the experimental results (EXP) and the simulation results (SIM). Despite some discrepancies between EXP and SIM,

they exhibit the same overall trend, with an average error of  $\pm 0.46^\circ\text{C}$ . In Fig. 14(b), EXP is compared to the prediction results (PRE) of prediction models, with the red bar indicating the error between EXP and PRE. EXP aligns with the trend observed in PRE, with average errors of  $0.53^\circ\text{C}$  for  $T_A$  and  $0.14$  for  $C_n$ . The consistency between EXP, SIM, and PRE suggests that the numerical model and prediction models utilized in this study are suitable for analyzing the melting performance of EHCPS-HPT.

### 3.3. New calculation method of snow-free ratio

To assess the snow-melting effectiveness of EHCPS-HPT, the primary evaluation metric used is the snow-free area ratio  $A_r$ . This ratio compares the equivalent snow-free area to the equivalent snow-covered area. In the simulation,  $A_r$  is calculated as the ratio of the number of points on the snow layer surface with a temperature greater than  $0^\circ\text{C}$  to the total number of points on the snow layer surface. However, the influences of the road surface condition, meltwater flow and meltwater infiltration are not considered in the simulation. Therefore, the simulation results will likely be larger than the experimental results [31]. To address this discrepancy, a new assessment metric  $\varphi$  is proposed, and its relationship with  $A_r$  is established to derive a modified snow-free ratio function, as shown in Eq. (15). The  $\varphi$  can be calculated from the simulation results.

$$\varphi = \begin{cases} 1, & 0.8 \leq A_r \leq 1 \\ -1, & 0 \leq A_r \leq 0.8 \end{cases} \quad (15)$$

Then using  $T_A$  and  $C_n$  as intermediate variables, a new evaluation function between  $\varphi$  and the four influencing parameters ( $s, d, P, v$ ) is shown as follows.

$$\begin{aligned} \varphi &= \text{sgn}(1.08T_A^2 - 0.59C_n^2 + 3.96T_A C_n - 8.10T_A - 2.24C_n - 10.82) \\ &= \text{sgn}[i \cdot j \cdot (s^2 + d^2 + P^2 + v^2 + s \cdot d + s \cdot P + s \cdot v + d \cdot P + d \cdot v + P \cdot v)] \end{aligned} \quad (16)$$



Fig. 13. Cement concrete slab experiments: (a) Temperature measuring points; (b) Temperature measurement; (c) Snow melting.

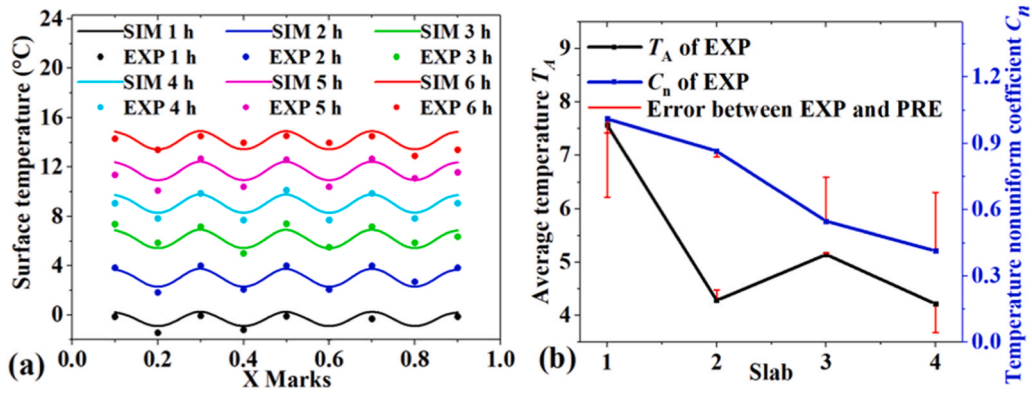


Fig. 14. The validation for the thermal simulation: (a) Comparison of the surface temperature between EXP and SIM under the condition that  $s=0.20$  m,  $d=0.10$  m,  $P=140$  W/m,  $v=0$  m/s, no accumulated snow; (b) Comparison of the  $T_A$  and  $C_n$  between EXP and PRE under the condition that  $P=40$  W/m,  $v=0$  m/s.

To further validate the applicability of the new calculation method, 180 schemes were generated by permuting the parameter levels outlined in Table 1 and introduced into Eq. (16). The calculated results were then compared with the simulation results, yielding an error rate of only 4.44 %. In Fig. 15, each scheme’s simulation value was compared with its corresponding value calculated using Eq. (16). When the simulation value equaled the value from Eq. (16), the black and red points coincided; otherwise, they did not align. The white coordinate zone encompasses all comparison results, while the blue zone highlights the errors. Among the 180 comparisons, only 8 resulted in errors. Consequently, Eq. (16) is deemed a reliable calculation equation for the snow-free ratio.

In this scenario, an operational strategy can be recommended based on the new calculation method. Firstly, calculate  $T_A$  and  $C_n$  based on the layout parameters ( $s$ ,  $d$ ), operational parameter ( $P$ ), and environmental parameter ( $v$ ). Next, compute  $\varphi$  using Eq. (16). Finally, determine the qualification of EHCPS-HPT by assessing whether  $\varphi$  equals 1 or  $-1$ . If  $\varphi = -1$ , it suggests that  $T_A$  and  $C_n$  need adjustment according to Eq. (16) and the analysis provided in Section 3.1. Given that adjusting  $v$  may be challenging, focusing on the efficient adjustment of  $s$  and  $P$  is recommended. This is because both  $T_A$  and  $C_n$  are highly sensitive to changes in  $s$  and  $P$ , as discussed in Section 3.1. Adjusting these parameters can effectively modify  $T_A$  and  $C_n$  to meet the desired criteria.

#### 4. Conclusions

Based on finite element simulations and experimental studies, this research has developed a new calculation method of snow-free ratio to address the technical bottleneck left by the traditional use of snow-free ratio in assessing snow-melting performance, which fails to accurately

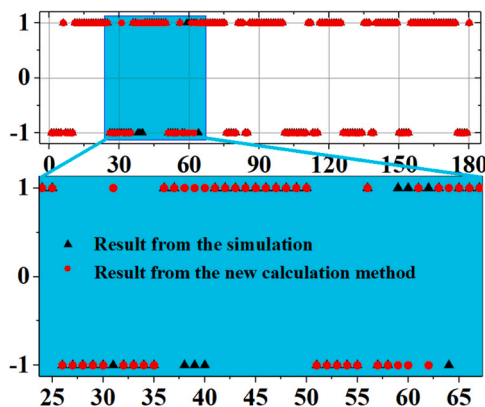


Fig. 15. The comparisons between the results from new calculation method and the results from the simulation.

reflect the unique wavy temperature distribution of EHCPS-HPT. This new method not only assesses the snow-melting performance of EHCPS-HPT but also aids in adjusting its operational strategies. These findings can guide the design and operation of EHCPS-HPT systems under heavy, moderate, or light snow conditions. The main conclusions can be summarized as follows:

- The finite element model of EHCPS-HPT is established and the effects of four parameters, including embedded spacing ( $s$ ), embedded depth ( $d$ ), heating power ( $P$ ) and wind velocity ( $v$ ), on the average temperature ( $T_A$ ) and temperature nonuniform coefficient ( $C_n$ ) of the pavement surface are investigated. In the analysis of the  $T_A$ , as the  $s$  and  $v$  increases,  $T_A$  decreases, and the rate of decrease also diminishes. As the  $d$  increases,  $T_A$  decreases, and the rate of decrease accelerates. As the  $P$  increases,  $T_A$  increases linearly. In the analysis of the  $C_n$ , except for  $s$ , the relationships between  $C_n$  and the other factors are similar to those for  $T_A$ . As  $s$  increases, the  $C_n$  initially decreases and then increases.
- In addition, the sensitivity analysis of four parameters was conducted using the Response Surface Method combined with the Monte Carlo Method. The results indicate that  $P$ ,  $v$ , and  $s$  are the key parameters impacting  $T_A$ , with influence probabilities of 58.76 %, 23.92 % and 14.51 % respectively. Meanwhile, it is clear that  $v$  is the dominant parameter affecting  $C_n$ , with an influence probability of 96.6 %, which is considerably higher than that of the other parameters.
- The prediction models for  $T_A$  and  $C_n$  are developed based on the thermal simulation results and the response surface methodology. In addition, the prediction models and numerical models are validated through snow-melting experiments. The experimental results and the simulation results exhibit the same overall trend, with an average error of  $\pm 0.46^\circ\text{C}$ . Meanwhile, experimental results align with the trend observed in the prediction models, with average errors of  $0.53^\circ\text{C}$  for  $T_A$  and  $0.14$  for  $C_n$ .
- The calculated results obtained from the new method were compared with the simulation results, yielding an error rate of only 4.44 %. In addition, adjusting  $s$  and  $P$  is the most efficient measure to adjust  $T_A$  and  $C_n$ , thus achieving good snow-melting performance.

This study is merely a starting point for improving the evaluation methods of heated systems for melting snow and ice, but the results are encouraging. Based on the significant findings of this research, there are still many areas worth further exploration to enhance our understanding. For instance, in the development of the finite element calculation model, the impact of the parameters of the heating system on pavement temperature, energy dissipation, and utilization rates during the dynamic snow melting process should be considered. Moreover, the evaluation method of snow-melting performance for electrically heated concrete pavement systems utilizing heating pipe technology proposed

in this study requires validation through more practical engineering projects.

### CRedit authorship contribution statement

**Fang Wang:** Writing – review & editing, Supervision, Data curation. **Chaoliang Fu:** Writing – review & editing, Writing – original draft, Visualization, Formal analysis. **Yangming Gao:** Validation, Writing – review & editing.

### Declaration of Competing Interest

The authors declare no conflict of interest.

### Data Availability

Data will be made available on request.

### Acknowledgements

This work was supported by the National Natural Science Foundation of China (Grant No. 52078177).

### References

- [1] M. Cai, et al., Evaluation of simulation uncertainty in accident reconstruction via combining response surface methodology and Monte Carlo method, *Transp. Res. Part C Emerg. Technol.* 48 (2014) 241–255.
- [2] X. Cao, et al., Feasibility assessment of implementing energy pile-based snowmelt system on a practical bridge deck in diverse climate conditions across China, *Energy* 290 (2024) 130317.
- [3] J. Choudhary, et al., Evaluation of engineering, economic and environmental suitability of waste filler incorporated asphalt mixes and pavements, *Road. Mater. Pavement Des.* 22 (2021) s624–s640.
- [4] Clarke J.A. *Energy Simulation in Building Design*, University of Strathclyde, Glasgow, Scotland, 1985.
- [5] J.W. Daniels, et al., Development of automated electrical heat grid for pavement snowmelt, *Therm. Sci. Eng. Prog.* 10 (2019) 169–178.
- [6] S. Debbarma, et al., Utilization of industrial and agricultural wastes for productions of sustainable roller compacted concrete pavement mixes containing reclaimed asphalt pavement aggregates, *Resour. Conserv. Recycl.* 152 (2020) 104504.
- [7] L. Fay, X.M. Shi, Environmental impacts of chemicals for snow and ice control: state of the knowledge, *Water Air Soil Pollut.* 223 (2012) 2751–2770.
- [8] C.L. Fu, et al., Exploring directional energy conversion behavior of electromagnetic-based multifunctional asphalt pavement, *Energy* 268 (2023) 126573.
- [9] C.L. Fu, et al., Comprehensive evaluation of thermally conductive functional layer on snow-melting performance for electric heating bridge system, *Cold Reg. Sci. Technol.* 219 (2024) 104099.
- [10] R.C. Gonzalez, *Digital image processing [M]*, Pearson education, India, 2009.
- [11] Y. Hassan, et al., Effects of runway deicers on pavement materials and mixes: comparison with road salt, *J. Transp. Eng.* 128 (2002) 385–391.
- [12] W.X. Jiao, et al., Optimization design and prediction of the snow-melting pavement based on electrical-thermal system, *Cold Reg. Sci. Technol.* 193 (2022) 103406.
- [13] Jorgensen, R. and Associates, 1964. *Non-Chemical Methods of Snow and Ice Control on Highway Structures*. National Cooperative Highway Research Program Report No.4, Highway Research Board, National Academy of Sciences, Washington.
- [14] W. Kim, et al., Effects of reinforcing fiber and microsilica on the mechanical and chloride ion penetration properties of latex-modified fiber-reinforced rapid-set cement concrete for pavement repair, *Adv. Mater. Sci. Eng.* 2018 (2018) 6839350.
- [15] K. Kupiec, et al., Heat transfer in horizontal ground heat exchangers, *Appl. Therm. Eng.* 75 (2015) 270–276.
- [16] Y. Lai, et al., Automatically melting snow on airport cement concrete pavement with carbon fiber grille, *Cold Reg. Sci. Technol.* 103 (2014) 57–62.
- [17] H. Li, et al., Analytic investigations of CNFP-based self-deicing road system on the deicing performance, *Cold Reg. Sci. Technol.* 103 (2014) 123–132.
- [18] W. Liu, *Research on Traffic Safety Technology under Adverse Climate in Mountainous Areas*, Chang'an University, Xi'an, China, 2015.
- [19] K. Liu, et al., The equivalent plasticity strain analysis of snow-melting heated pavement concrete exposed to inner elevated temperatures, *Constr. Build. Mater.* 137 (2017) 66–75.
- [20] K. Liu, et al., Multi-objective optimization of the design and operation for snow-melting pavement with electric heating pipes, *Appl. Therm. Eng.* 122 (2017) 359–367.
- [21] D. Lu, et al., Sustainable microwave-heating healing asphalt concrete incorporating functional aggregates and waste ferrite, *Transp. Res. Part D Transp. Environ.* 129 (2024) 104117.
- [22] R.M. Mitchell, A synoptic analysis of hazardous weather at Heathrow 2005-2022 and its impact on airport operations, *Weather* 79 (2024) 10–16.
- [23] A. Pandey, B. Kumar, A comprehensive investigation on application of microsilica and rice straw ash in rigid pavement, *Constr. Build. Mater.* 252 (2019) 119053.
- [24] A. Pandey, B. Kumar, Utilization of agricultural and industrial waste as replacement of cement in pavement quality concrete: a review, *Environ. Sci. Pollut. Res.* 29 (2022) 24504–24546.
- [25] L. Quante, et al., Regions of intensification of extreme snowfall under future warming, *Sci. Rep.* 11 (2021) 16621.
- [26] M. Saleem, et al., Development, testing, and implementation strategy of a translucent concrete-based smart lane separator for increased traffic safety, *J. Constr. Eng. Manag.* 143 (2017) 04016129.
- [27] M. Saleem, N.I. Blaisi, Development, testing, and environmental impact assessment of glow-in-the-dark concrete, *Struct. Concr.* 20 (2019) 1792–1803.
- [28] M. Saleem, A. Hosoda, Development and testing of glow-in-the-dark concrete based raised pavement marker for improved traffic safety, *J. Civ. Eng. Manag.* 27 (2021) 278–287.
- [29] R.S. Tang, et al., Estimates of clear night sky emissivity in the Negev Highlands, Israel, *Energy Convers. Manag.* 45 (2004) 1831–1843.
- [30] H.J. Wang, et al., Experimental investigation of ice and snow melting process on pavement utilizing geothermal tail water, *Energy Convers. Manag.* 49 (2008) 1538–1546.
- [31] H.J. Wang, Z.H. Chen, Study of critical free-area ratio during the snow-melting process on pavement using low-temperature heating fluids, *Energy Convers. Manag.* 50 (2009) 157–165.
- [32] Williams G.P., 1974. *Heat Requirements of Snow Melting Systems in Canada*. 1st National Conference on Snow and Ice Control Symposium, Ottawa, Ontario, Canada, 179–197.
- [33] C.G. Xu, et al., Uncertainty and sensitivity analysis for models with correlated parameters, *Reliab. Eng. Syst. Saf.* 93 (2008) 1563–1573.
- [34] C.G. Xu, et al., A general First-Order global sensitivity analysis method, *Reliab. Eng. Syst. Saf.* 93 (2008) 1060–1071.
- [35] S.N. Zamanabadi, et al., Ambient-cured alkali-activated slag paste incorporating micro-silica as repair material: effects of alkali activator solution on physical and mechanical properties, *Constr. Build. Mater.* 137 (2019) 66–75.
- [36] C.Y. Zhang, et al., Advanced multiple response surface method of sensitivity analysis for turbine blisk reliability with multi-physics coupling, *Chin. J. Aeronaut.* 29 (2016) 962–971.
- [37] H.M. Zhao, et al., Concrete slab installed with carbon fiber heating wire for bridge deck deicing, *J. Transp. Eng.* 136 (2010) 500–509.
- [38] H.M. Zhao, et al., Concrete pavement deicing with carbon fiber heating wires, *Cold Reg. Sci. Technol.* 65 (2011) 413–420.
- [39] W.K. Zhao, et al., Snow melting on a road unit as affected by thermal fluids in different embedded pipes, *Sustain. Energy Technol. Assess.* (2021).